

# Modeling solar energetic particle transport in 3D background solar wind: Influences of the compression regions

Wenwen Wei<sup>a,b</sup>, Fang Shen<sup>a,b,c,\*</sup>, Zicai Yang<sup>a,b</sup>, Lulu Zhao<sup>d</sup>, Yang Wang<sup>c</sup>, Pingbing Zuo<sup>c</sup>, Jie Zhang<sup>e</sup>

<sup>a</sup> SIGMA Weather Group, State Key Laboratory of Space Weather, National Space Science Center, Chinese Academy of Sciences, Beijing, 100190, China

<sup>b</sup> College of Earth Sciences, University of Chinese Academy of Sciences, Beijing, 100049, China

<sup>c</sup> HIT Institute of Space Science and Applied Technology, Shenzhen, 518055, China

<sup>d</sup> Department of Physics and Space Sciences, Florida Institute of Technology, Melbourne, FL, 32901, USA

<sup>e</sup> Department of Physics and Astronomy, George Mason University, Fairfax, 22030, Virginia, USA

## ARTICLE INFO

### Keywords:

Solar energetic particle  
Magnetohydrodynamics  
Magnetic field  
Solar wind  
Interplanetary transport

## ABSTRACT

In modeling the transport process of solar energetic particles (SEPs) in the heliosphere, previous simulation works often simplify the solar wind velocity as radial and constant, and treat the magnetic field as Parker spiral. In order to fully understand the effect of solar wind velocity and interplanetary magnetic field on the particles' transport process, a realistic background solar wind and magnetic field is required. In this work, we use the focused transport model to investigate the transport of SEPs in the solar wind velocity and magnetic field generated by the 3D high-resolution MHD model with a six-component grid. We find that in the uncompressed solar wind, the time intensity profiles of energetic particles show similar trend in both the MHD background and the Parker magnetic field assumption. However, the simulated SEP flux displays an enhancement in the decay phase when a compression region sweeps past the local observer. Through investigating various effects, we find that the magnetic focusing effect is primarily responsible for the intensity enhancement, suggesting that the magnetic focusing effect has an important influence on the transport of SEPs. Further, we show that the magnetic focusing could also be effective in large heliocentric distances.

## 1. Introduction

Solar energetic particle (SEP) events are flux enhancements of high-energy solar particles, which could be produced by solar flares or coronal mass ejections. The SEP events, if sufficiently intense, could cause damage to spacecraft and limit human activities in space (Reames, 1999, 2013). It is desirable to develop accurate forecast ability of SEP events, and for this purpose, numerical simulations play an important role in modeling and specifying the evolution of energetic particle events and improving our understanding of these events on a global scale.

There have been many such studies of SEP events (Ruffolo, 1995; Qin et al., 2006; Zhang et al., 2009) based on standard, simplified solar wind conditions of a spiral magnetic field configuration with constant radial solar wind velocity (Parker, 1958). However, recent studies suggest the SEP events frequently occur in disturbed solar wind, implying the necessity to study them accurately based on MHD modeling

of real background solar wind conditions (e.g., Sokolov et al., 2004; Kocharov et al., 2009; Kozarev et al., 2010; Schwadron et al., 2014). The technique approach is to combine a magnetohydrodynamic (MHD) model that provides the background conditions with a particle model that investigates the behavior of SEPs. With such an approach, substantial efforts have been made to combine the particle model with two-dimensional (2D) (Lario et al., 1998; Li et al., 2003) or three-dimensional (3D) MHD model (Kocharov et al., 2009; Schwadron et al., 2014; Bain et al., 2016). In our study, we also combine a 3D MHD model developed by our team with a particle model to study the SEP behavior in the simulated interplanetary environment.

Energetic particles associated with Corotating Interaction Regions (CIRs) also attract much attention in recent years (Mason and Sanderson, 1999; Richardson, 2004; Zhao et al., 2016). CIRs are formed where fast solar wind catches up with slow solar wind in the interplanetary space (e.g., Crooker et al., 1999; Huang et al., 2016). Both observations and simulations indicate that such structured solar wind

\* Corresponding author. SIGMA Weather Group, State Key Laboratory of Space Weather, National Space Science Center, Chinese Academy of Sciences, Beijing, 100190, China.

E-mail address: [fshen@spaceweather.ac.cn](mailto:fshen@spaceweather.ac.cn) (F. Shen).

<https://doi.org/10.1016/j.jastp.2018.11.012>

Received 13 July 2018; Received in revised form 19 November 2018; Accepted 20 November 2018

Available online 28 November 2018

1364-6826/ © 2018 Elsevier Ltd. All rights reserved.

can significantly modify the behavior of energetic particles (Bryant et al., 1965; Reames et al., 1991; Giacalone et al., 2002; Kocharov et al., 2003; Richardson, 2004; Wu et al., 2014; Zhao et al., 2016). Most of these works focus on the acceleration of energetic particles by the forward and/or reverse shocks bounding a CIR via the first order Fermi acceleration mechanism, and the acceleration is capable of modulating sub-MeV nucleon<sup>-1</sup> particles (Fisk and Lee, 1980; Zhao et al., 2016; Li, 2017). Moreover, Giacalone et al. (2002) suggested that the compression region without shocks can also accelerate particles to about 10 MeV nucleon<sup>-1</sup> through a process similar to diffusive shock acceleration. Kocharov et al. (2003) presented the first modeling of SEP events inside corotating compression regions, and found that CIRs at about 1 AU could re-accelerate SEPs. Besides, both Giacalone et al. (2002) and Kocharov et al. (2003) emphasized the importance of magnetic mirroring in the inner heliosphere, suggesting that a local magnetic mirror could be a source of CIR particle events. In general, transport processes, which include effects such as magnetic focusing or mirroring, convection with solar wind, adiabatic cooling, and diffusion processes, are key elements of physics that control many features of energetic particles intensities (e.g., Ruffolo, 1995; Qin et al., 2006; Zhang et al., 2009; Kocharov et al., 2009; Mason et al., 2012; Wang et al., 2012).

However, the contribution by CIRs to the SEP transport needs to be further investigated for the following reasons. First, the compression region in previous studies was constructed within Parker spiral field, while background solar wind generated by MHD model could provide a different or maybe more realistic condition. Second, the magnetic focusing effect is investigated generally within 2 AU based on the variations of focusing length, but an overall distribution of focusing length is still lacking, which may lead to an incomplete estimation of the contribution from magnetic focusing within such a short distance. Third, the transport of SEPs in the decay phase of “SEP events” at a larger heliocentric distance has not been well investigated before, but will be addressed in our study.

In this work, we will first describe how we develop the model of combining a 3D MHD model with a particle transport model, and then use the combined model to study the SEP evolution with a focus on investigating the influences of compression regions on the transport of SEPs in the decay phase of “SEP events”. The 3D solar wind is generated by solving the MHD equations with Corona-interplanetary Total Variation Diminishing (COIN-TVD) model, which uses a modified Total Variation Diminishing/Lax-Friedrichs (TVD/LF) type scheme (Feng et al., 2003; Shen et al., 2007, 2009) in a Sun-centered spherical coordinate system  $(r, \theta, \varphi)$ . Next, we combine the 3D background solar wind generated from the COIN-TVD MHD with the SEP transport model described by Zhang et al. (2009) (hereafter this coupling model will be called MHD-SEP model). The SEP model solves the Fokker-Planck transport equation with a time-backward Markov stochastic method (Zhang et al., 2009). The SEP model is assumed in a fixed reference frame, in which the spacecraft is roughly stationary. Finally, we employ the MHD-SEP model to study the transport of SEPs in both uncompressed solar wind and solar wind with compression regions. For the sake of simplicity, we concentrate on the propagation of high-energy ( $E \geq 20$  MeV) SEPs in the 3D background solar wind with no disturbances from interplanetary coronal mass ejection (ICME) structures or their shocks. We will focus on the intensity variations of energetic protons. The paper is structured as follows: In Section 2, we introduce the MHD model, SEP model and their combination of the MHD-SEP model. Section 3 describes the results from the MHD-SEP model in the transport process of SEPs in both the uncompressed solar wind and the compression region. Summary is given in Section 4.

## 2. The coupled MHD-SEP transport model

In the following, we describe the MHD model for the simulations of 3D-structured solar wind, and the particle transport model for investigating the SEP behaviors in the interplanetary space. Subsequently,

we discuss the coupling of the two models to establish MHD-SEP model.

### 2.1. MHD model

The steady state 3D background solar wind is constructed by solving the ideal MHD equations with high resolution TVD/LF scheme (Feng et al., 2003; Shen et al., 2007, 2009, 2014) in spherical coordinates with a six-component grid that covers the entire spherical surface (Feng et al., 2010, 2014a, b). The ideal MHD equations can be written in a rotating frame as follows:

$$\frac{\partial \rho}{\partial t} + \nabla \cdot (\rho \mathbf{V}) = 0 \quad (1)$$

$$\frac{\partial \rho \mathbf{V}}{\partial t} + \nabla \cdot \left[ \left( P + \frac{B^2}{2\mu_0} \right) \mathbf{I} + \rho \mathbf{V} \mathbf{V} - \frac{\mathbf{B} \mathbf{B}}{\mu_0} \right] = -\frac{\rho G M_s}{r^2} \frac{\mathbf{r}}{r} + \mathbf{f} \quad (2)$$

$$\frac{\partial \mathbf{B}}{\partial t} + \nabla \cdot (\mathbf{V} \mathbf{B} - \mathbf{B} \mathbf{V}) = 0 \quad (3)$$

$$\frac{\partial P}{\partial t} + \nabla \cdot (\rho \mathbf{V}) + (\gamma - 1) P \nabla \cdot \mathbf{V} = 0 \quad (4)$$

where  $\rho = n(m_p + m_e)$  is the mass density,  $n$  is number density,  $m_p$  is the proton mass and  $m_e$  is the electron mass,  $\mathbf{V}$  is solar wind velocity vector,  $\mathbf{B}$  is magnetic field vector,  $\mathbf{I}$  is the unit tensor,  $\mathbf{f} = -\boldsymbol{\Omega}' \times [\boldsymbol{\Omega}' \times \mathbf{r} + 2\boldsymbol{\Omega}' \times \mathbf{V}]$  is the centrifugal force, we choose a constant solar angular rotation speed  $\boldsymbol{\Omega}' = 14.71$  degday<sup>-1</sup>, which corresponds to the sidereal rotation period of 24.47 days (Snodgrass and Ulrich, 1990; Shen et al., 2018),  $P = 2nkT$  is the thermal pressure,  $k$  is the Boltzmann constant,  $T$  is the temperature,  $\mu_0$  is the vacuum permeability,  $G$  is the gravitational constant,  $M_s$  is the solar mass,  $r$  is the heliocentric radial distance,  $\gamma$  is the ratio of specific heats and is taken to be 1.46 here (Totten et al., 1995; Shen et al., 2018).

The computational domain of the mesh system is  $0.1 \text{ AU} \leq r \leq 8 \text{ AU}$ ,  $0 \leq \theta \leq \pi$ , and  $0 \leq \varphi \leq 2\pi$  in radial, meridional and azimuthal direction, respectively. We use a composite mesh consisting of six identical component meshes designed to envelop a spherical surface with partial overlap on their boundaries (Feng et al., 2010). The advantages of using the six-component composite mesh include the avoidance of coordinate singularity near the poles, the improvement of our computational efficiency, and the easy implementation of the inner boundary conditions according to different requirements as described by Feng et al. (2010). Furthermore, the employment of six-component grid in our simulations also reduces high numerical dissipation. The mesh system will be introduced in more detail in section 2.3.2.

The algorithm employed produces a predictor step and corrector step with a second-order accuracy. In order to keep the numerical error of  $\nabla \cdot \mathbf{B}$  in an allowable level, the artificial diffusive approach is used (Shen et al., 2014).

The inner boundary is chosen to be located at 0.1 AU, and a set of empirical formulae to derive the inner boundary conditions for the MHD simulations are given as follows. The radial magnetic field ( $B_r$ ) is provided with the potential field source surface (PFSS) model by utilizing magnetograms obtained by the Global Oscillation Network Group (GONG) of the National Solar Observatory (NSO; <ftp://gong2.nso.edu/mnt/oQR/mqs/>). We use the empirical relationship for the radial flow velocity,  $V_r$  (), derived from the WSA coronal solar wind model (Arge et al., 2003; McGregor et al., 2011).

$$V_r = V_s + \frac{V_m}{(1 + f_s)^{\alpha_1}} \left[ 1 - 0.8 \exp \left\{ -\left( \frac{\theta_b}{\alpha_2} \right)^{\alpha_3} \right\} \right]^{\alpha_4} \quad (5)$$

Here,  $f_s$  is the flux tube expansion factor,  $\theta_b$  is the minimum angular separation between an open magnetic field foot point and its nearest coronal hole boundary.  $V_s$  sets the minimum possible solar wind speed while  $V_m$  determines the maximum speed. Besides  $f_s$  and  $\theta_b$ , there are six

free parameters in the boundary conditions, which can be tuned to simulate the solar wind for different phases of solar cycle in our simulation. The meridional and azimuthal magnetic field ( $B_\theta$  and  $B_\varphi$ ) and the meridional and azimuthal flow velocities ( $V_\theta$  and  $V_\varphi$ ) are assumed to be zero. A constant momentum flux is assumed to derive the mass density ( $\rho$ ), and the pressure ( $P$ ) is chosen to assure the total pressure (sum of thermal and magnetic pressures) is uniform on the source surface.

## 2.2. Particle transport model

The modulation of SEPs in the interplanetary medium is described by the Fokker-Planck transport equation as shown in the following (Skillington, 1971; Qin et al., 2006; Zhang et al., 2009):

$$\frac{\partial f}{\partial t} + (\mu v \mathbf{b} + \mathbf{V}) \cdot \nabla f - \frac{\partial}{\partial \mu} D_{\mu\mu} \frac{\partial f}{\partial \mu} + \frac{d\mu}{dt} \frac{\partial f}{\partial \mu} + \frac{dp}{dt} \frac{\partial f}{\partial p} = 0 \quad (6)$$

Where  $f(\mathbf{x}, \mu, p, t)$  is the gyro phase-averaged distribution function of SEPs as a function of spatial location  $\mathbf{x}$ , particle momentum  $p$ , pitch-angle cosine  $\mu$ , and time  $t$ .  $v$  is the particle speed,  $\mathbf{b}$  is the magnetic field unit vector,  $\mathbf{V}$  is the solar wind velocity,  $D_{\mu\mu}$  is the pitch-angle diffusion coefficient, and  $L_B = -(\mathbf{b} \cdot \nabla \ln B)^{-1}$  is the magnetic focusing length. The adiabatic cooling effect is described by

$$\frac{dp}{dt} = -p \left[ \frac{\mu}{v} \mathbf{b} \cdot \left( \frac{\partial \mathbf{V}}{\partial t} + \mathbf{V} \cdot \nabla \mathbf{V} \right) + \frac{(1 - \mu^2)}{2} (\nabla \cdot \mathbf{V} - \mathbf{b} \mathbf{b} : \nabla \mathbf{V}) + \mu^2 \mathbf{b} \mathbf{b} : \nabla \mathbf{V} \right] \quad (7)$$

and the time evolution of  $\mu$  is written as

$$\frac{d\mu}{dt} = \mu \mathbf{b} \cdot \left( \frac{\partial \mathbf{b}}{\partial t} + \mathbf{V} \cdot \nabla \mathbf{b} \right) - \frac{1 - \mu^2}{v} \mathbf{b} \cdot \left( \frac{\partial \mathbf{V}}{\partial t} + \mathbf{V} \cdot \nabla \mathbf{V} \right) + \frac{(1 - \mu^2)v}{2L_B} + \frac{\mu(1 - \mu^2)}{2} (\nabla \cdot \mathbf{V} - 3\mathbf{b} \mathbf{b} : \nabla \mathbf{V}) \quad (8)$$

The colon “:” in this paper represents double dot product, e.g.,  $\mathbf{b} \mathbf{b} : \nabla \mathbf{V} = b_i b_j \frac{\partial v_j}{\partial x_i}$ . We solve the focused transport equation with the time-backward Markov stochastic method (Zhang, 1999; Qin et al., 2006; Zhang et al., 2009). Particles with a power law spectrum  $\alpha = 3.0$  are injected at the inner boundary. The boundary condition of Equation (6) at the interface is set as the injected source of SEPs (Reid, 1964; Qin et al., 2006), i.e.  $f_b(\mathbf{x}, \mu, p, t)|_{r=R_{in}} = \frac{C E_k^{-\alpha}}{t_i p^2} e^{-\left(\frac{t}{t_c} + \frac{t}{t_i}\right)}$ , where  $E_k$  is source particle's kinetic energy,  $p$  is the particle momentum,  $t_c$  and  $t_i$  are time constants that indicate the rise and decay timescales of the source injection profile, respectively. We set  $t_c = 0.08333$  day and  $t_i = 0.25$  day in the calculation. Thus, the particles are uniformly injected in the inner boundary in our simulations. Then the solution of Equation (6) is the expectation value of the boundary values at the exit points:

$$f(\mathbf{x}, \mu, p, t) = \frac{\sum_{i=1}^N f_b(\mathbf{x}_e, \mu_e, p_e, t_e)}{N} \quad (9)$$

Where  $\mathbf{x}_e, \mu_e, p_e, t_e$  represent parameters when the stochastic trajectories hit the inner boundary,  $N$  is the total number of injected particles. The first order flux anisotropy is

$$A = \frac{3 \int_{-1}^1 f(\mu) \mu d\mu}{\int_{-1}^1 f(\mu) d\mu} \quad (10)$$

Table 1 lists the model parameters used in the Parker magnetic field simulations. Except the inner and outer boundaries, the other parameters are the same as in Zhang et al. (2009). In this model, the parallel mean free path,  $\lambda_{\parallel}$ , is related to the particle pitch-angle diffusion coefficient  $D_{\mu\mu}$  (Jokipii, 1966; Earl, 1974), i.e.  $\lambda_{\parallel} = \frac{3v}{8} \int_{-1}^1 \frac{(1 - \mu^2)^2}{D_{\mu\mu}} d\mu$ . Furthermore, the parallel mean free path projected in the radial direction  $\lambda_r = \lambda_{\parallel} \cos^2 \psi$  is assumed to be a constant (Bieber et al., 1994), where  $\psi$  is the angle of the local magnetic field direction to the radial line.

## 2.3. MHD-SEP model: the combination of MHD and particle transport model

The MHD modeling provides a 3D interplanetary structure, which is the base for SEP transport simulations. The combination of the two models, which is crucial for such purpose, needs to handle several challenges due to the differences between the two models, e.g., the simulation region, the grid mesh, the reference frame, etc. In this section, we will present the details of how the combination of MHD-SEP model is handled in the following.

### 2.3.1. The simulation region

The solar wind velocity and magnetic field used in the SEP model are provided by the COIN-TVD MHD model. In general, the outer boundary of SEP model could extend to tens of AU (Zhang et al., 2009). However, the MHD model still has some existing limitations, including the computational capacity and the requirement to obtain a solution with a fine grid resolution that converges with a reasonable time, thus the MHD solution has to be limited to 8 AU in the radial direction. In this study, 8 AU is far enough to investigate energetic particles behaviors, so our MHD-SEP model will choose the outer boundary to be 8 AU. Besides, the inner boundary of MHD model is located at 0.1 AU, where the solar wind speed is super-magnetoacoustic. Then, any perturbations in the simulation domain cannot travel towards the Sun and the constant boundary conditions can be used (Wiengarten et al., 2014). Moreover, as we primarily study the transport of SEPs in the compression regions, we can directly input a source of SEPs at the inner boundary as described in section 2.2. Consequently, we choose the inner boundary of the MHD-SEP model to be 0.1 AU.

### 2.3.2. The computational mesh

As described in section 2.1, the simulated domain in MHD model is  $0.1 \text{ AU} \leq r \leq 8 \text{ AU}$ ,  $0 \leq \theta \leq \pi$ , and  $0 \leq \varphi \leq 2\pi$ . The grid network is chosen to be  $501(r) \times 181(\theta) \times 361(\varphi)$ . The uniform grids are used in latitudinal and longitudinal directions, with  $\Delta\theta = 1^\circ$  and  $\Delta\varphi = 1^\circ$ . The radial direction is prescribed as equal-ratio grid mesh, with  $\Delta r_{i-1} = \varepsilon r_{i-1}$  ( $i = 2, 3, \dots, N_r$ ). In this work,  $\varepsilon$  is the equal-ratio coefficient and is set to be 0.008847. With spatial discretization, we define the grids of mesh system in MHD model as:  $r_i = r_{i-1} + \varepsilon r_{i-1}$  ( $i = 2, 3, \dots, N_r$ ),  $\theta_j = \frac{(j-1)\pi}{N_\theta - 1}$  ( $j = 1, 2, \dots, N_\theta$ ),  $\varphi_k = \frac{(k-1)2\pi}{N_\varphi - 1}$  ( $k = 1, 2, \dots, N_\varphi$ ),  $N_r, N_\theta$  and  $N_\varphi$  represent the grid numbers in the radial, meridional and azimuthal directions, respectively. Here,  $r_1 = 0.1 \text{ AU}$ ,  $N_r = 501$ ,  $N_\theta = 181$  and  $N_\varphi = 361$ . Besides, we use  $(r_i, \theta_j, \varphi_k)$  for the position of the particle in MHD-SEP model, and we can get the subscripts ( $i', j', k'$ ) with  $i' = \text{int}\left(\frac{\log(r_i/r_1)}{\log(1+\varepsilon)}\right) + 1$ ,  $j' = \text{int}\left(\frac{\theta_j(N_\theta - 1)}{\pi}\right) + 1$ ,  $k' = \text{int}\left(\frac{\varphi_k(N_\varphi - 1)}{2\pi}\right) + 1$ . Here “int” function returns an integer type value. Therefore, when we find the position of a particle, the MHD background condition at that position can be traced. If only the parameters on the grid point ( $i', j', k'$ ) are chosen, the numerical error could be large. Therefore, the parameters on the adjacent eight grid points should be used to derive the background parameters with a trilinear interpolation method, as shown in Fig. 1.

### 2.3.3. Concerns on reference frames

It should be emphasized that the momentum and pitch angle in the transport equation are defined in the solar wind frame, while the spatial coordinates are defined in the fixed reference frame. Besides, the background solar wind obtained in the solar corotating frame, which is used in our MHD simulations, is still time-dependent in the fixed frame. Although time-dependent terms exist in  $dp/dt$  and  $d\mu/dt$  (see Equation (7) and Equation (8)), they can be excluded due to the fact that they are minor terms in comparison with other terms.

In Equation (7), the time-dependent term is  $\frac{\mu}{v} \mathbf{b} \cdot \left( \frac{\partial \mathbf{V}}{\partial t} + \mathbf{V} \cdot \nabla \mathbf{V} \right)$ , which has a smaller order of magnitude when compared with the other two terms. An example of the term  $\mu^2 \mathbf{b} \mathbf{b} : \nabla \mathbf{V}$ , the magnitude analysis of

**Table 1**  
Model parameters in the simulations.

Parameters	Formula	Initial Values
Inner Boundary	$r = R_{in}$	$R_{in} = 0.1 \text{ AU}$
Outer Boundary	$r = R_{out}$	$R_{out} = 8 \text{ AU}$
Solar Rotation	$\Omega = 2\pi/T$	$T = 27.27 \text{ d}$
Solar Wind	$\mathbf{V} = V\mathbf{e}_r$	$V = 400 \text{ km s}^{-1}$
Parker magnetic Field	$\mathbf{B} = \frac{B_0}{r^2}\mathbf{e}_r - \frac{B_0\Omega \sin\theta}{rV}\mathbf{e}_\varphi$	$B_0 = 3.54 \text{ nT}$
Pitch Angle Diffusion	$D_{\mu\mu} = D_0 v p^{-2/3} (1 - \mu^2) \{  \mu ^{q-1} + h \} k(x)$	$h = 0.2, q = 5/3$ $k(x) = \cos^2\psi = (B_r/B)^2$

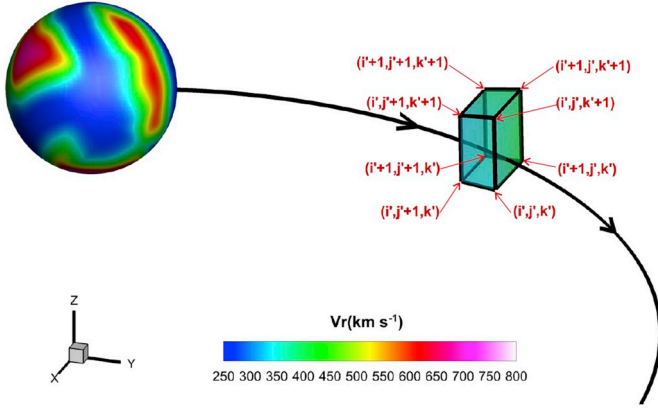


**Fig. 1.** The illustration of the grid points used in the model. The spherical shell represents the inner boundary of the model ( $R_{in} = 0.1 \text{ AU}$ ), with the color denotes the solar wind speed that is derived from the WSA model. The black solid line with arrow illustrates the magnetic field line. The parameters on the eight adjacent grid points, as marked by  $i', j'$  and  $k'$ , are used to calculate the background parameters.

them is shown in Equation (11), where  $L$  is the spatial scale (AU) and  $t$  is the time scale of the solar wind (day). Therefore, the time-dependent term is much smaller as the particle speed  $v$  is comparable to light speed. Similarly, the time-dependent term  $\left(\frac{\partial b}{\partial t} + \mathbf{V} \cdot \nabla b\right)$  in Equation (8) can also be ignored. As a result, we can rewrite the variations of  $dp/dt$  and  $d\mu/dt$  in Equation (12) and Equation (13).

$$\frac{\mu}{v} \mathbf{b} \cdot \left( \frac{\partial \mathbf{V}}{\partial t} + \mathbf{V} \cdot \nabla \mathbf{V} \right) \sim \frac{\mu b}{v} \left( \frac{V}{t} + \frac{VV}{L} \right) \sim \frac{L/t + V}{\mu^2 \mathbf{b} \mathbf{b} : \nabla \mathbf{V}} \sim \frac{L/t + V}{v} \quad (11)$$

$$\frac{dp}{dt} = -p \left[ \frac{(1 - \mu^2)}{2} (\nabla \cdot \mathbf{V} - \mathbf{b} \mathbf{b} : \nabla \mathbf{V}) + \mu^2 \mathbf{b} \mathbf{b} : \nabla \mathbf{V} \right] \quad (12)$$

$$\frac{d\mu}{dt} = \frac{(1 - \mu^2)v}{2L_B} + \frac{\mu(1 - \mu^2)}{2} (\nabla \cdot \mathbf{V} - 3\mathbf{b} \mathbf{b} : \nabla \mathbf{V}) \quad (13)$$

Accordingly, we transform the background physical parameters from the co-rotating frame into the fixed frame. For a fixed point, we assume  $\varphi_c$  is equal to  $\varphi_f$  at the initial time in both frames, then  $\varphi_c = \varphi_f - \Omega \Delta t$  after time  $\Delta t$ , where  $\Omega$  is the solar rotation speed given in Table 1. Here the subscripts “c” and “f” refer to the solar corotating frame and the fixed reference frame, respectively. In addition, the distribution of the injected particles at time  $t$  corresponds to the initial backward time  $s = 0$ . If we assume X-axis in solar corotating frame is coincided with that in the fixed frame, the background at the time  $(t - s)$  is needed when particles run backward. At this time, we need a rotation in longitudinal direction to get the distribution at time  $(t - s)$ , i.e.  $\Delta t = -s$ , then we can get the transformed results, namely  $\varphi_c = \varphi_f + \Omega s$ ,  $r_c = r_f$ ,  $\theta_c = \theta_f$ . Solar wind speed and magnetic field are derived from the Lorentz transformation,  $V_{rf} \approx V_{rc}$ ,  $V_{\theta f} \approx V_{\theta c}$ ,  $V_{\varphi f} \approx V_{\varphi c} + \Omega r$ ;  $B_{rf} \approx B_{rc}$ ,  $B_{\theta f} \approx B_{\theta c}$ ,  $B_{\varphi f} \approx B_{\varphi c}$ .

After combining the MHD model with the particle transport model, we can now simulate the transport of SEPs in a more realistic 3D background solar wind. Generally, the particles are injected from a source near the Sun, then propagate in the interplanetary medium, and their propagation is governed by the focused transport equation which includes essentially all the particle transport mechanisms. We use boundary value  $f_b(\mathbf{x}, \mu, p, t)$  to model the particles’ injection from the source. In our model, the transport processes are decoupled from the acceleration processes. Once acceleration processes are under consideration, we can directly input a source of accelerated particles as a product of either CME shock or solar flare to avoid the problems of particle injection and acceleration (Zhang et al., 2009; Zhao et al., 2016). Moreover, no ICME or shocks are included in our background solar wind. Therefore, in this paper, we primarily focus on the transport processes by setting distributed boundary values as described in section 2.2 in the following simulations.

### 3. Simulation results and discussion

#### 3.1. Uncompressed solar wind conditions

Using the MHD-SEP model, we first select a period of uncompressed solar wind to study the SEP behaviors, and compare it with the results under the circumstance of Parker spiral magnetic field. The observations in Carrington rotation (CR) 2066, which begins from 2008 January 25, during the last extended solar minimum serve as the input to the MHD model to obtain the 3D background solar wind. One CIR in this CR has been reconstructed with a 3D model by Wood et al. (2010), but we here focus on an uncompressed region. Fig. 2 shows the distribution of the radial solar wind speed  $V_r$  () within 8 AU (left panel) and 1 AU (right panel) in the ecliptic plane. The color bar in the left panel indicates the solar wind speed. In both panels, the black curves plot the magnetic field lines and the arrows on top show the polarity. The black solid circle in the right panel represents the observation point at (1AU,  $\pi/2$ ,  $\pi/9$ ) in spherical coordinates. In the right panel, the area between the dashed red curves in the longitudinal range of  $66^\circ$  is a period of relatively uncompressed solar wind. We study the SEP behaviors in this area. Fig. 3(a) shows the results from the particle transport model. From top to bottom, the panels show the simulated omnidirectional fluxes for 30 MeV protons over five days, the simulated solar wind speed, magnetic field strength, proton number density, temperature, and pressure variations at the observation point. The plasma properties shown in panels (ii) to (vi) show relatively small variations, indicating a period of uncompressed solar wind. In panel (i), the red line shows the particles flux profile obtained from the MHD background solar wind, and the black line denotes the flux profile using the Parker spiral magnetic field with a fixed radial solar wind speed of 400 . It is clear that the omnidirectional flux decreases faster within MHD background solar wind than that in the Parker spiral magnetic field, but both of them show a similar trend. The faster flux decrease may be associated with the strengthened adiabatic cooling effect caused by solar wind speed (Lario et al., 1997; Qin et al., 2006).

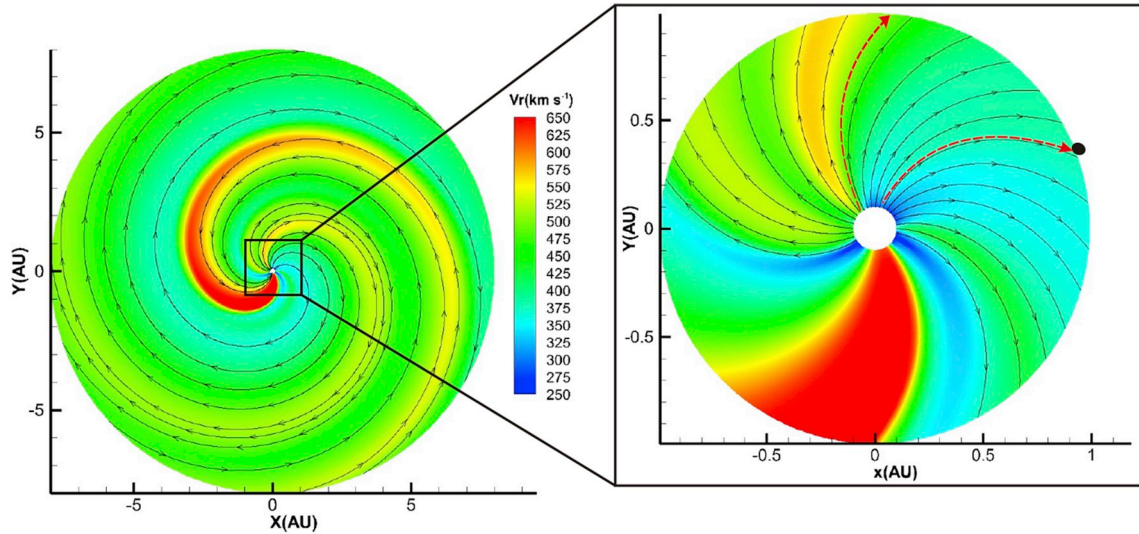


**Fig. 2.** The distribution of the calculated MHD steady-state radial speed  $V_r$  ( $\text{km s}^{-1}$ ) for CR2066 within 8 AU (left panel) and 1 AU (right panel) in the ecliptic plane. The color contours in the left panel represent the radial solar wind speed. Streamlines and the black solid circle in the right panel denote the magnetic field lines and the observation point, respectively. The region between the two red dashed lines in the right panel is the uncompressed solar wind region chosen for this study.

### 3.2. Compression region conditions

We then investigate the effects of the solar wind compression regions on the transport of energetic particles in the 3D background solar wind. In this part of work, we would like to choose a CR with different solar activity, and select compression regions without negative divergence of plasma flow, which may involve with acceleration mechanism as suggested by Giacalone et al. (2002). We obtain the solar wind velocity and magnetic field from the MHD model constrained by the observations in CR 2145, which begins from 2013 December 19, during the rising phase of solar cycle 24. Fig. 4 shows the distribution of  $V_r$  within 8 AU (left panel) and 1 AU (right panel) in the ecliptic plane, in the similar format as Fig. 2. The black solid circle at  $(1\text{AU}, \pi/2, \pi/2)$  in

the right panel marks the observer. The chosen region is marked by the red dashed curves ranging about  $66^\circ$  in longitude. The interaction between fast and slow solar wind in the right part of the chosen region suggests that it is a compression region, which is consistent with the longitudinal variations of solar wind parameters as shown in Fig. 3(b) (more discussions present in the following section). Fig. 5(a) shows the proton omnidirectional fluxes and anisotropies at three different energies, 20 MeV, 30 MeV, 50 MeV, in the black solid line, red dotted line and blue dashed line, respectively. This Figure shows that one extra peak of the omnidirectional fluxes occurs in the decay phase between days 2.5 and 3.5, at different energies. This phenomenon exists in different compression regions in the 3D simulated background solar wind. We will discuss this extra peak phenomenon in the following section.

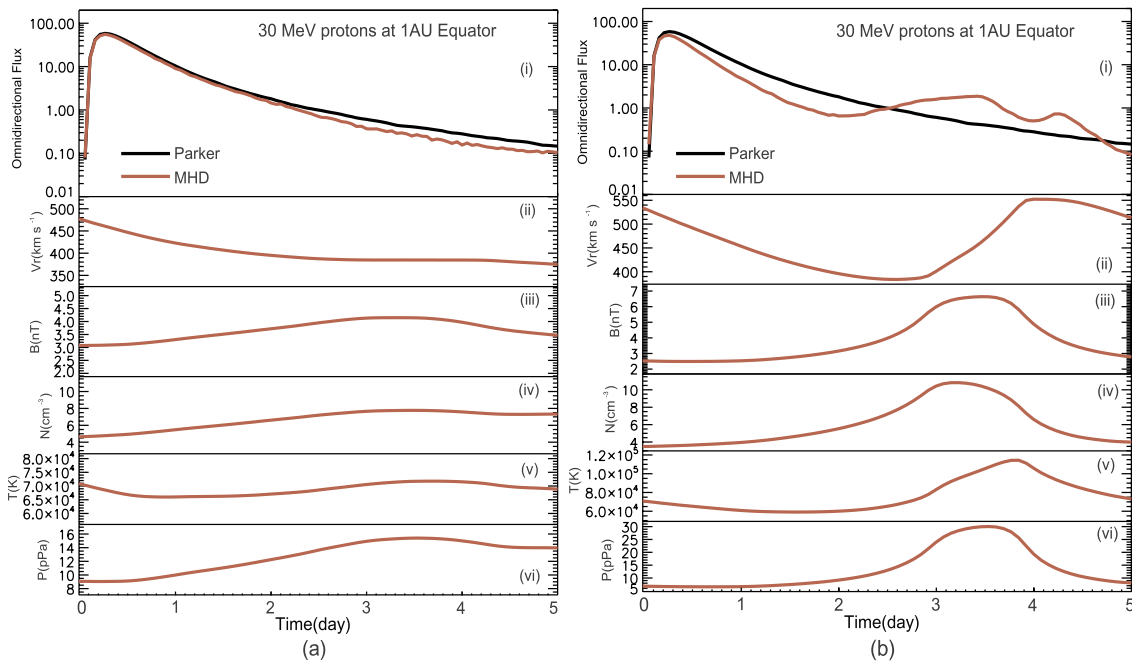


**Fig. 3.** (a) Omnidirectional flux with two different background field and solar wind parameters under uncompressed solar wind conditions; (b) Omnidirectional flux with two different background field and solar wind parameters in the compression region. Panels from top to bottom: omnidirectional fluxes of Parker solar wind (black) and MHD solar wind (red), the radial speed  $V_r$  ( $\text{km s}^{-1}$ ), the magnetic field strength  $|B|$  (nT), the proton number density ( $\text{cm}^{-3}$ ), the proton temperature (K) and the pressure (pPa) from the MHD simulations. The solar wind conditions in (a) and (b) are derived from Figs. 2 and 4, respectively.

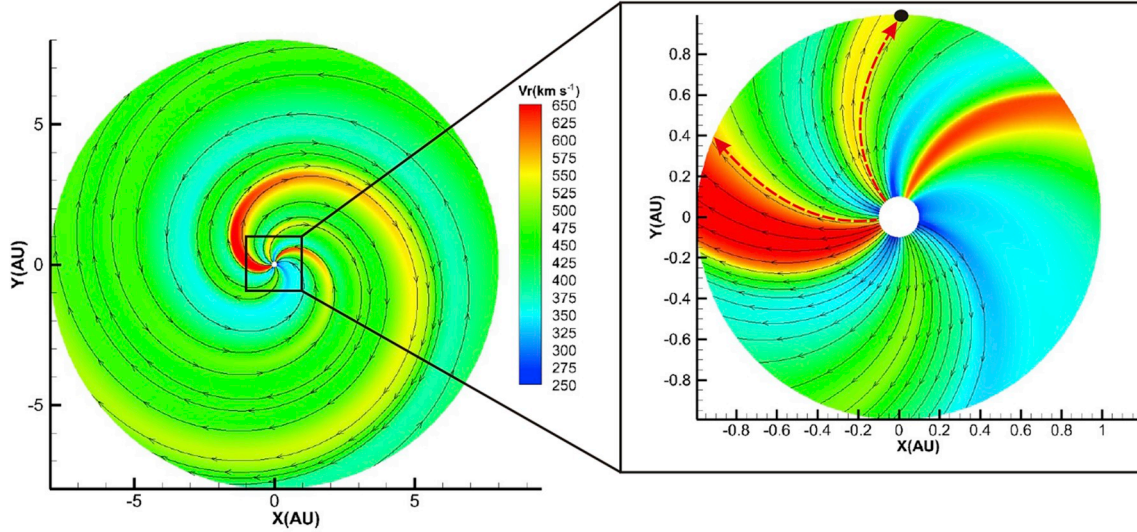


Fig. 4. The distribution of the calculated MHD steady-state radial speed  $V_r$  ( $\text{km s}^{-1}$ ) for CR2145 within 8 AU (left panel) and 1 AU (right panel) in the ecliptic plane. The color contours in the left panel represent the radial solar wind speed. Streamlines and the black solid circle in the right panel denote the magnetic field lines and the observation point, respectively.

### 3.3. Discussion

First of all, we analyze the influence exerted by the adiabatic cooling effect on the particles flux variations. Because we focus on the transport of SEPs rather than acceleration, simulation results at other energies are also similar to those of 30 MeV protons. This allows us choose 30 MeV as an example for further examination. Fig. 5(b) gives a comparison of omnidirectional flux and anisotropy between the results with and without adiabatic cooling effect. It shows that the adiabatic cooling effect, shown in Fig. 5(b) by a black solid line, only lowers the total flux rather than alters the enhancement pattern. As a result, we conclude that the adiabatic cooling effect is not responsible for the enhancement in the decay phase.

Fig. 3(b) shows the omnidirectional flux using different background field at energy of 30 MeV (panel i), and also the MHD background parameters (panel ii to vi) that pass through the observer at 1 AU (the same background conditions as in Fig. 5(a) and the same format as in Fig. 3(a)). Red line in panel (i) represents the flux derived from the MHD background condition, which increases to an even higher level than that obtained from the simplified Parker spiral magnetic field and fixed solar wind speed at 400 as shown by the black line. From this Figure, it is obvious that the flux enhancement appears evidently in a gradual compression region, which is characterized by the enhanced solar wind speed, magnetic field strength, proton number density, and pressure. In the following, we will further investigate why such region could enhance the particles flux.

Since the adiabatic cooling effect doesn't lead to the result, we further analyze the particle transport mechanisms of streaming along magnetic field lines and convection with the solar wind, pitch-angle diffusion and magnetic focusing effect as shown by the second, third and fourth term in Equation (6). Previous study showed that solar wind speed had an effect on the adiabatic cooling and could change the overall level of the flux but not the trend with time (Qin et al., 2006). Furthermore, the mechanism of streaming along magnetic field lines and pitch-angle diffusion can be assumed to be parallel spatial diffusion. As a result, pitch-angle diffusion and magnetic focusing effect could be the possible reasons. The variation of  $\mu$  by time is described by the following Equation (14). Since solar wind speed is much smaller than the particle speed, the pitch-angle diffusion and magnetic focusing become the overwhelming terms as shown in Equation (15).

$$d\mu(s) = \sqrt{2 \max(D_{\mu\mu}, 0)} dw(s) + \left[ \frac{\partial D_{\mu\mu}}{\partial \mu} - \frac{(1 - \mu^2(s))v}{2L_B} - \frac{\mu(s)(1 - \mu^2(s))}{2} (\mathbf{v} \cdot \mathbf{V} - 3\mathbf{b}\mathbf{b} : \nabla \mathbf{V}) \right] ds \quad (14)$$

$$d\mu(s) \approx \sqrt{2 \max(D_{\mu\mu}, 0)} dw(s) + \left[ \frac{\partial D_{\mu\mu}}{\partial \mu} - \frac{(1 - \mu^2(s))v}{2L_B} \right] ds \quad (15)$$

Pitch-angle diffusion is caused by the magnetic fluctuations, and it is related to the parallel mean free path (Qin et al., 2004; Zhang et al., 2009). Magnetic focusing effect is important in the SEP transport (Tautz et al., 2012; Wang and Qin, 2016) and it is related with  $L_B$ . Previous works often assumed a constant magnetic focusing length  $L_B$ , which is defined as  $L_B = -(\mathbf{b} \cdot \nabla \ln B)^{-1}$  (Roelof, 1969; Tautz et al., 2012). In a Parker spiral magnetic field,  $L_B$  increases with heliocentric distance. But the variation of  $L_B$  would be more complicated in a realistic large-scale heliospheric field (Wang and Qin, 2016). The competition between pitch-angle diffusion and magnetic focusing effect is determined by the ratio of mean free path to  $L_B$ .

First, we analyze the effect of pitch-angle diffusion. Fig. 5(c) displays a comparison of omnidirectional flux and anisotropy with different parallel mean free paths  $\lambda_{\parallel}$ . The black lines represent the results by using the  $\lambda_{\parallel}$  obtained from the MHD magnetic field, and the red dot-dashed lines denote the results with the modified  $\lambda_{\parallel}$ . As shown in section 2.2,  $\lambda_{\parallel}$  is derived from pitch-angle diffusion coefficient  $D_{\mu\mu}$ , which is a spatial correlation function related to  $k(x)$ . In comparison, we modify  $\lambda_{\parallel}$  by replacing  $k(x)$  derived from MHD magnetic field with that from Parker spiral magnetic field. From Fig. 5(c), we can see that the omnidirectional flux under the condition of  $\lambda_{\parallel}$  obtained from MHD magnetic field is higher than that from Parker magnetic field. Due to the angle  $\psi$  decreases in compression regions, which leads the corresponding increases of pitch-angle diffusion  $D_{\mu\mu}$ , the parallel mean free path  $\lambda_{\parallel}$  decreases accordingly. Thus, the omnidirectional flux decays more slowly as the parallel diffusion coefficient becomes smaller.

Generally, the smaller the parallel diffusion coefficient is, the slower the flux decays, which is consistent with Fig. 5(c). Since the influence exerted by the change of parallel diffusion coefficient is similar to that of the adiabatic cooling effect, i.e., change the flux level but not the trend, the magnetic focusing effect is more likely to be responsible for the flux enhancement in the decay phase. Fig. 6(a) shows the normalized distribution of the reciprocal magnetic focusing length, i.e.  $(L_B)^{-1}$ , within 8 AU in the ecliptic plane. The chosen region is marked by the

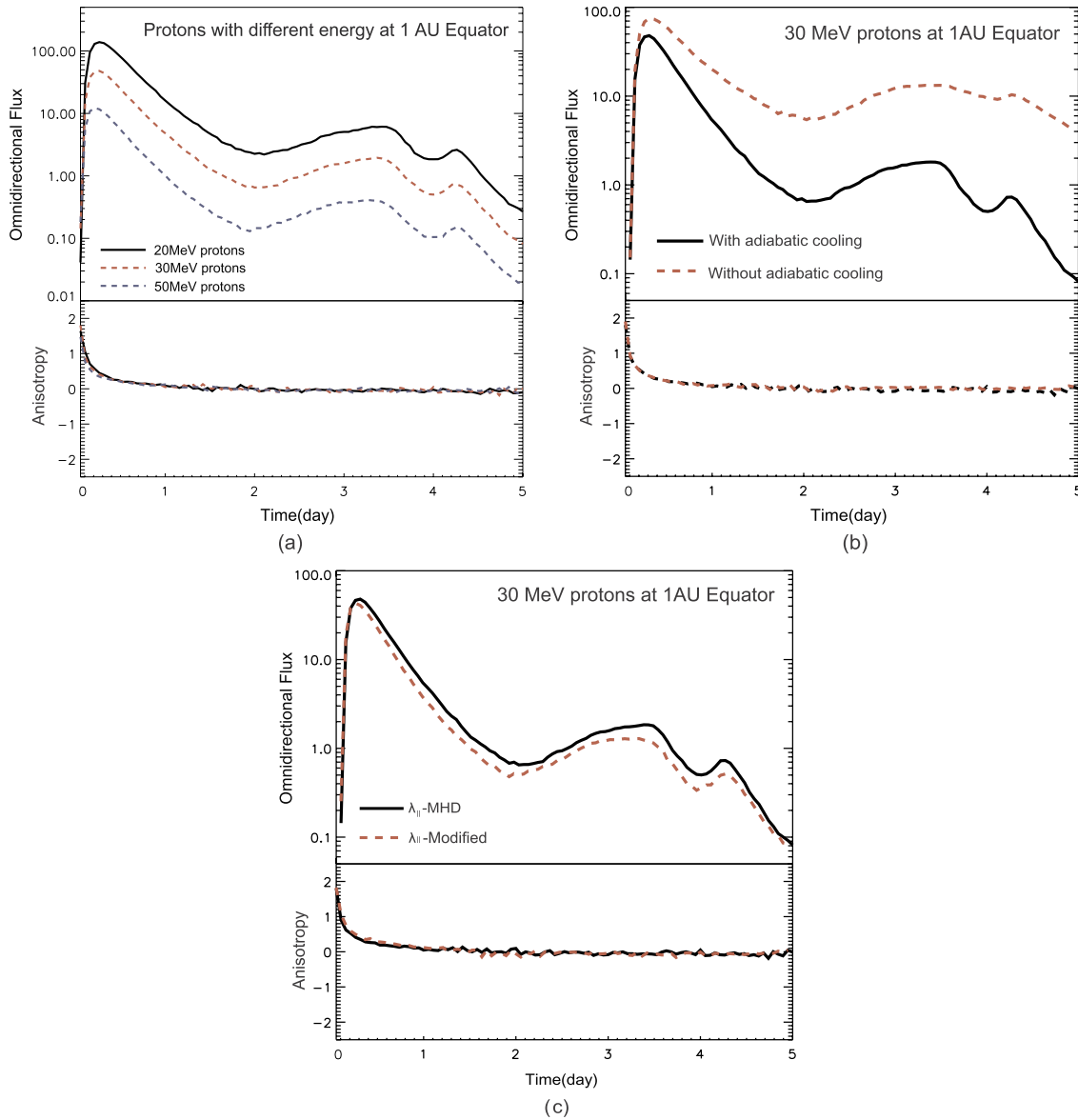


**Fig. 5.** (a) The comparison of omnidirectional flux and anisotropy at three different energies with the same simulated background field. (b) The comparison of omnidirectional flux and anisotropy solved from the transport equation with and without adiabatic cooling. (c) The comparison of omnidirectional flux and anisotropy with different  $\lambda_{||}$ .

black magnetic field lines ranging about  $66^\circ$  in longitude.  $(L_B)^{-1}$  generally describes the strength of magnetic focusing or mirroring effect. Generally, the smaller value of  $(L_B)^{-1}$ , the stronger magnetic mirroring effect. This Figure shows that  $(L_B)^{-1}$  varies between positive and negative values, which are different from only positive values in Parker magnetic field. In the Parker assumption,

$$\mathbf{b} = \mathbf{B}/B = \cos \beta \mathbf{e}_r - \sin \beta \mathbf{e}_\varphi, \quad \cos \beta = \frac{B_r}{B}, \quad \sin \beta = -\frac{B_\varphi}{B} \quad (16)$$

the magnetic focusing term can be written as  $\frac{(1-\mu^2)v}{2L_B} = \frac{(1-\mu^2)v \cos \beta (1+\cos^2 \beta)}{2r}$ . Due to the positive values of  $v$  and  $\cos \beta$  as introduced in section 2.2, the focusing term is greater than zero, unless it is equal to zero when  $\mu = \pm 1$ , i.e. the pitch angle of particles is  $0^\circ$  or  $180^\circ$ , and the focusing effect would consequently force the particles to flow parallel to the magnetic field lines. On the other hand, the values of  $(L_B)^{-1}$  could be positive or negative in MHD conditions, implying that particles may be mirrored back and observed when they experience a strong magnetic mirroring effect that indicated by small  $(L_B)^{-1}$ . Moreover, a small  $(L_B)^{-1}$  region generally corresponds to a compression

region, and it is reasonable to see particles to be reflected back in such regions. [Kocharov et al. \(2003\)](#) simulated the intensity profiles of SEPs in compression regions that constructed in Parker field. They found that a trap-like structure of the interplanetary magnetic field modifies the SEP intensity-time profiles and the magnetic trapping effect makes intensity-time profiles very flat. They accounted for the flux enhancement primarily to the acceleration of CIRs. In our results, we have already excluded the acceleration mechanism, thus we conclude that the magnetic focusing effect is the main reason that leads to the flux enhancement in the decay phase.

[Fig. 7](#) presents the variations of  $(L_B)^{-1}$  (green line) and proton number density  $N$  (blue line), where  $(L_B)^{-1}$  and  $N$  are in units of  $\text{AU}^{-1}$  and  $\text{cm}^{-3}$ , respectively. Different panels correspond to different heliocentric distances. The gray shaded area in each panel presents the variations of  $(L_B)^{-1}$  and  $N$  in our focused region. The compression regions, as suggested by enhanced  $N$ , are generally related to small  $(L_B)^{-1}$  values, implying that the magnetic mirroring effect associates closely to the compression regions. [Giacalone et al. \(2002\)](#) find negative focusing length in the compression regions, and [Kocharov et al. \(2003\)](#) further

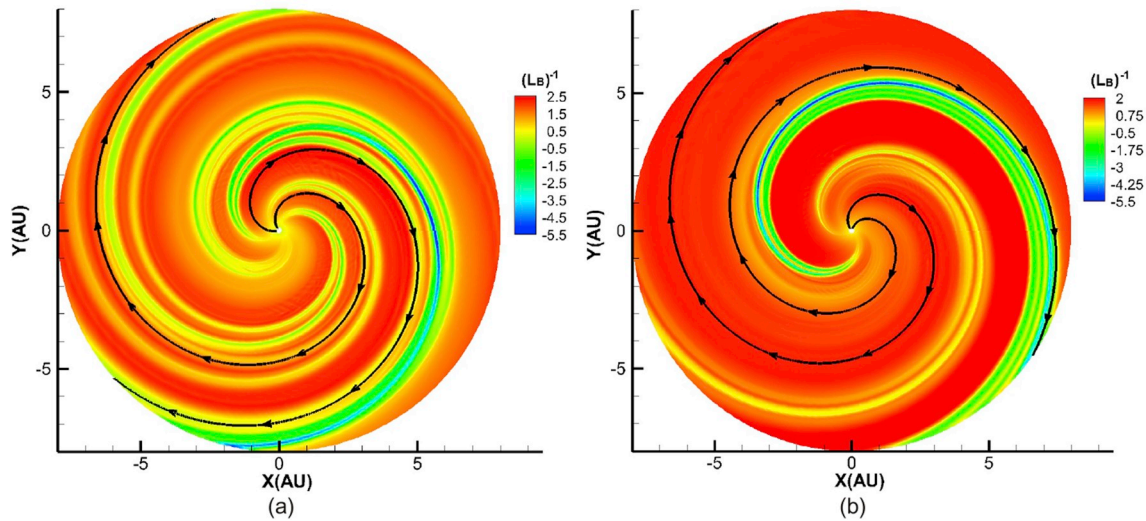


Fig. 6. (a)The distribution of the calculated  $(L_B)^{-1}$  at ecliptic plane during CR2145; (b)The distribution of the calculated  $(L_B)^{-1}$  at ecliptic plane during CR2066. The areas between the black magnetic field lines in the longitudinal range of  $66^\circ$  represent the interested regions for examining SEP behaviors.

emphasize the local magnetic mirroring effect based on the occurrence of negative  $(L_B)^{-1}$  values at around 1 AU. Therefore, our results confirm their results. In addition, both Figs. 6 and 7 further denote that small and/or even negative  $(L_B)^{-1}$  values could appear in large heliocentric distances and dominate an area that is not tiny, implying that magnetic mirroring effect may also be effective beyond 1 AU.

We have also investigated  $(L_B)^{-1}$  in the uncompressed solar wind conditions as shown in Fig. 6(b), in comparison with that of compression regions shown in Fig. 6(a). This Figure indicates that  $(L_B)^{-1}$  has varied values in different spatial positions, and significant negative values occur in the compression regions, where the simulated flux (not shown) increases in the decay phase. However,  $(L_B)^{-1}$  stays nearly uniform in uncompressed solar wind region which is marked by the black magnetic field lines ranging about  $66^\circ$  in longitude, and the values of  $(L_B)^{-1}$  are generally positive and not too small, implying that particles

may not be mirrored back by magnetic mirroring effect in these uncompressed solar wind regions.

Fig. 8 sketches the possible process of magnetic mirroring effect. The red and blue lines represent positive and negative values of  $(L_B)^{-1}$ , respectively. The purple balls that mainly distribute between the red and blue lines generally have small  $(L_B)^{-1}$ , implying strong compression regions. The two black dash lines with arrows show the region that sweeps over the observer at 1 AU, and black ball shows the observation point as shown in the right panel of Fig. 4. When the particles transport in the compression regions, magnetic mirroring effect could reflect some particles back like a mirror as  $(L_B)^{-1}$  value becomes small and/or even negative. Therefore the observer detects a flux enhancement.

Besides, there are still some concerns about the flux enhancement in the decay phase. First, it seems there is another small flux enhancement after day 4 as shown in Fig. 3(b). There are two possible reasons. On

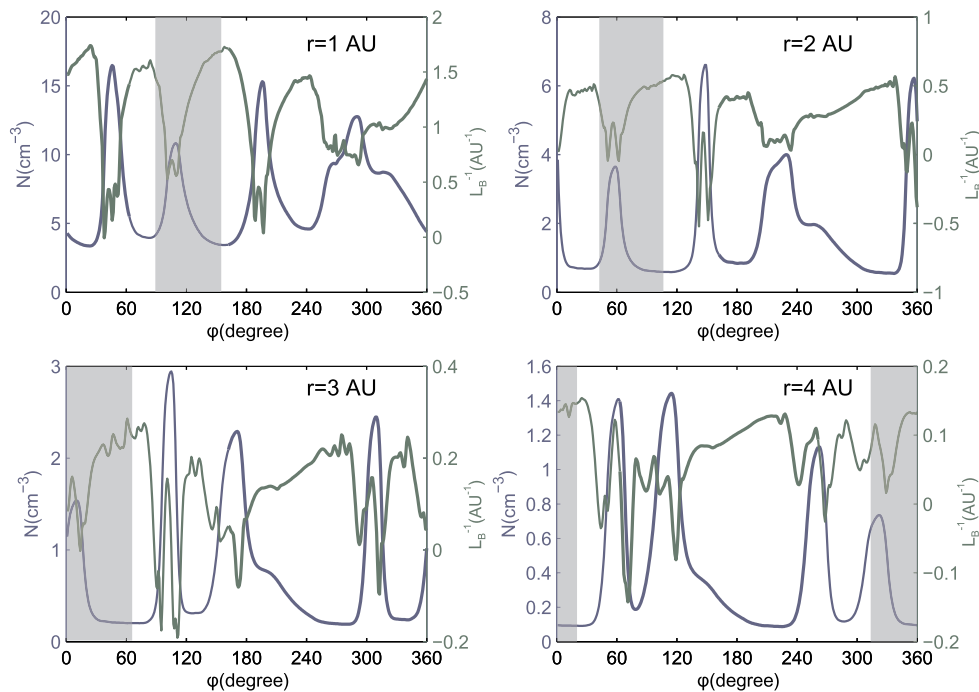
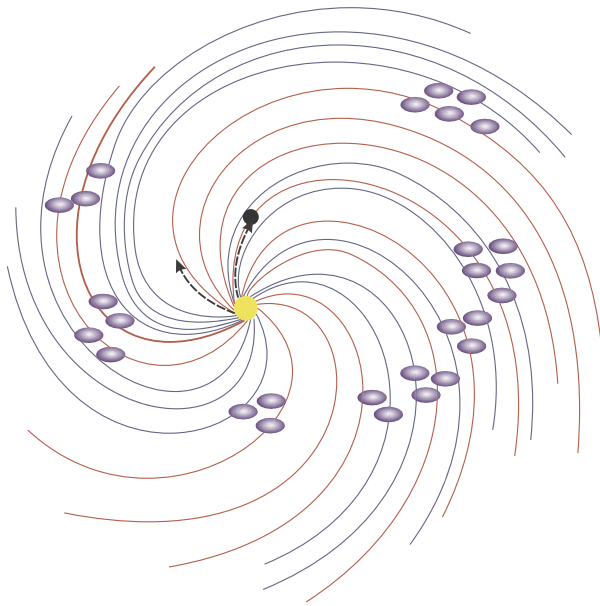


Fig. 7. The variations of  $N$  and  $(L_B)^{-1}$  at different heliocentric distances during CR2145. The blue lines and green lines represent  $N$  and  $(L_B)^{-1}$ , respectively. The gray shaded areas represent the interested regions for examining SEP behaviors.



**Fig. 8.** A cartoon showing possible regions where magnetic mirroring effects might occur and be efficient. The red and blue lines represent positive and negative values of  $(L_B)^{-1}$ , respectively. The purple balls imply strong compression regions. The two black dash lines with arrows show the region that sweeps over the observer (black ball) at 1 AU.

one hand, from Fig. 6(a) and Fig. 7 it seems that two regions with low  $(L_B)^{-1}$  values are adjacent to each other, implying the other flux enhancement could also be caused by magnetic mirroring effect that related to low  $(L_B)^{-1}$  values. However, the plasma data do not show two adjacent compression regions, suggesting that one compression region may include different low  $(L_B)^{-1}$  regions to mirror particles, or the plasma data can not show fine structures due to their current low resolutions. On the other hand, there may be some non-uniform structures in the simulated MHD magnetic field, which may contribute to the other flux enhancement. Second, the efficiency of magnetic mirroring effect on flux enhancement still need further investigations. It is difficult to estimate the efficiency of magnetic mirroring effect, because the magnitude is a result of collective effect of different transport factors. For example, adiabatic cooling effect would lower the flux enhancement, but smaller parallel diffusion coefficient could magnify it. In the future, we will try to simulate real events to estimate the contributions of different factors.

#### 4. Summary

We have reported on our study of the transport process of SEPs in the 3D solar wind velocity and magnetic field obtained from the MHD model. After the brief introduction of the MHD model and SEP model used, the combination of these two models is described in some details to establish the MHD-SEP model for investigating the transport process of SEPs. With the MHD-SEP model, we study the influence of interplanetary structures, mainly the compression regions, on SEP time intensity profiles and parallel diffusion coefficients.

We have explored the similarity and contrast of the transport of SEPs in uncompressed solar wind conditions versus compression regions. We find that the particles have a similar behavior in uncompressed solar wind as that in Parker spiral magnetic field, but the omnidirectional flux of SEP has an enhancement in the decay phase in compression regions. The analysis shows that magnetic mirroring effect is primarily responsible for the intensity enhancement based on the investigation of the reciprocal magnetic focusing length, i.e.  $(L_B)^{-1}$ . The variation of  $(L_B)^{-1}$  in realistic background solar wind shows that

magnetic mirroring effect could reflect the particles back to the observer in the compression regions, when  $(L_B)^{-1}$  has a small or even a negative value.

In this study, we present the distributions of  $(L_B)^{-1}$  in the ecliptic plane with 3D background solar wind conditions, and also propose that magnetic mirroring may also be effective in large heliocentric distances. This study confirms that the solar wind velocity and magnetic field in the compression regions would have a profound influence on the transport of SEPs. The MHD-SEP model also has potential for case studies of space weather events in the future.

#### Acknowledgments

The data for this work are available at the official websites of the Global Oscillation Network Group (GONG) of the National Solar Observatory (NSO; <http://gong.nso.edu/>). The work was carried out at the National Supercomputer Center in Tianjin, China, and the calculations were performed on TianHe-1 (A). We acknowledge the use of them. This work is jointly supported by grants from the National Natural Science Foundation of China (41374188, 41474152, 41231068, 41531073 and 41774184) and the Specialized Research Fund for State Key Laboratories. FS is also supported by the National Program for Support of Top-notch Young Professionals.

#### Appendix A. Supplementary data

Supplementary data to this article can be found online at <https://doi.org/10.1016/j.jastp.2018.11.012>.

#### References

- Arge, C.N., Odstrcil, D., Pizzo, V.J., Mayer, L.R., 2003. Improved method for specifying solar wind speed near the Sun. In: Velli, M., Bruno, R., Malara, F., Buccì, B. (Eds.), *Solar Wind Ten*, pp. 190–193. <https://doi.org/10.1063/1.1618574>. volume 679 of American Institute of Physics Conference Series.
- Bain, H.M., Mays, M.L., Luhmann, J.G., Li, Y., Jian, L.K., Odstrcil, D., 2016. Shock connectivity in the August 2010 and July 2012 solar energetic particle events inferred from observations and ENLIL modeling. *Astrophys. J.* 825, 1. <https://doi.org/10.3847/0004-637X/825/1/1>.
- Bieber, J.W., Matthaeus, W.H., Smith, C.W., Wanner, W., Kallenrode, M.-B., Wibberenz, G., 1994. Proton and electron mean free paths: the Palmer consensus revisited. *Astrophys. J.* 420, 294–306. <https://doi.org/10.1086/173559>.
- Bryant, D.A., Cline, T.L., Desai, U.D., McDonald, F.B., 1965. Continual acceleration of solar protons in the MeV range. *Phys. Rev. Lett.* 14, 481–484. <https://doi.org/10.1103/PhysRevLett.14.481>.
- Crooker, N.U., Gosling, J.T., Bothmer, V., Forsyth, R.J., Gazis, P.R., Hewish, A., Horbury, T.S., Intriligator, D.S., Jokipii, J.R., Kóta, J., Lazarus, A.J., Lee, M.A., Lucek, E., Marsch, E., Posner, A., Richardson, I.G., Roelof, E.C., Schmidt, J.M., Siscoe, G.L., Tsurutani, B.T., Wimmer-Schweingruber, R.F., 1999. CIR morphology, turbulence, discontinuities, and energetic particles. In: Balogh, A., Gosling, J.T., Jokipii, J.R., Kallenbach, R., Kunow, H. (Eds.), *Corotating Interaction Regions*. Springer Netherlands, Dordrecht, pp. 179–220.
- Earl, J.A., 1974. The diffusive idealization of charged-particle transport in random magnetic fields. *Astrophys. J.* 193, 231–242. <https://doi.org/10.1086/153152>.
- Feng, X., Wu, S.T., Wei, F., Fan, Q., 2003. A class of TVD type combined numerical scheme for MHD equations with a survey about numerical methods in solar wind simulations. *Space Sci. Rev.* 107, 43–53. <https://doi.org/10.1025/547016708>.
- Feng, X., Xiang, C., Zhong, D., Zhou, Y., Yang, L., Ma, X., 2014a. SIP-CESE MHD model of solar wind with adaptive mesh refinement of hexahedral meshes. *Comput. Phys. Commun.* 185, 1965–1980.
- Feng, X., Yang, L., Xiang, C., Wu, S.T., Zhou, Y., Zhong, D.K., 2010. Three-dimensional solar WIND modeling from the Sun to earth by a SIP-CESE MHD model with a six-component grid. *Astrophys. J.* 723, 300. <https://doi.org/10.1088/0004-637X/723/1/300>.
- Feng, X., Zhang, M., Zhou, Y., 2014b. A new three-dimensional solar wind model in spherical coordinates with a six-component grid. *Astrophys. J. Suppl.* 214, 6. <https://doi.org/10.1088/0067-0049/214/1/6>.
- Fisk, L.A., Lee, M.A., 1980. Shock acceleration of energetic particles in corotating interaction regions in the solar wind. *Astrophys. J.* 237, 620–626. <https://doi.org/10.1086/157907>.
- Giacalone, J., Jokipii, J.R., Kóta, J., 2002. Particle acceleration in solar wind compression regions. *Astrophys. J.* 573, 845–850. <https://doi.org/10.1086/340660>.
- Huang, J., Liu, Y.C.-M., Klecker, B., Chen, Y., 2016. Coincidence of heliospheric current sheet and stream interface: implications for the origin and evolution of the solar wind. *J. Geophys. Res.* 121, 19–29. <https://doi.org/10.1002/2015JA021729>.

- Jokipii, J.R., 1966. Cosmic-Ray propagation. I. Charged particles in a random magnetic field. *Astrophys. J.* 146, 480. <https://doi.org/10.1086/148912>.
- Kocharov, L., Kovaltsov, G.A., Torsti, J., Anttila, A., Sahla, T., 2003. Modeling the propagation of solar energetic particles in corotating compression regions of solar wind. *J. Geophys. Res.* 108, 1404. <https://doi.org/10.1029/2003JA009928>.
- Kocharov, L., Pizzo, V.J., Odstrcil, D., Zwickl, R.D., 2009. A unified model of solar energetic particle transport in structured solar wind. *J. Geophys. Res.* 114, A05102. <https://doi.org/10.1029/2008JA013837>.
- Kozarev, K., Schwadron, N.A., Dayeh, M.A., Townsend, L.W., Desai, M.I., PourArsalan, M., 2010. Modeling the 2003 Halloween events with EMMREM: energetic particles, radial gradients, and coupling to MHD. *Space Weather* 8, S00E08. <https://doi.org/10.1029/2009SW000550>.
- Lario, D., Sanahuja, B., Heras, A.M., 1997. Modeling the interplanetary propagation of 0.1–20 MeV shock-accelerated protons. I - effects of the adiabatic deceleration and solar wind convection. *Adv. Space Res.* 20, 115. [https://doi.org/10.1016/S0273-1177\(97\)00492-4](https://doi.org/10.1016/S0273-1177(97)00492-4).
- Lario, D., Sanahuja, B., Heras, A.M., 1998. Energetic particle events: efficiency of interplanetary shocks as 50 keV <math>E < 100</math> MeV proton accelerators. *Astrophys. J.* 509, 415–434. <https://doi.org/10.1086/306461>.
- Li, G., 2017. Particle acceleration and transport in the inner heliosphere. *Sci. China Earth Sci.* 60, 1440–1465. <https://doi.org/10.1007/s11430-017-9083-y>.
- Li, G., Zank, G.P., Rice, W.K.M., 2003. Energetic particle acceleration and transport at coronal mass ejection-driven shocks. *J. Geophys. Res.* 108, 1082. <https://doi.org/10.1029/2002JA009666>.
- Mason, G., Sanderson, T., 1999. CIR associated energetic particles in the inner and middle heliosphere. *Space Sci. Rev.* 89, 77–90. <https://doi.org/10.1023/A:1005216516443>.
- Mason, G.M., Li, G., Cohen, C.M.S., Desai, M.I., Haggerty, D.K., Leske, R.A., Mewaldt, R.A., Zank, G.P., 2012. Interplanetary propagation of solar energetic particle heavy ions observed at 1 AU and the role of energy scaling. *Astrophys. J.* 761, 104. <https://doi.org/10.1088/0004-637X/761/2/104>.
- McGregor, S.L., Hughes, W.J., Arge, C.N., Owens, M.J., Odstrcil, D., 2011. The distribution of solar wind speeds during solar minimum: calibration for numerical solar wind modeling constraints on the source of the slow solar wind. *J. Geophys. Res.* 116, A03101. <https://doi.org/10.1029/2010JA015881>.
- Parker, E.N., 1958. Dynamics of the interplanetary gas and magnetic fields. *Astrophys. J.* 128, 664–676. <https://doi.org/10.1086/146579>.
- Qin, G., Zhang, M., Dwyer, J.R., 2006. Effect of adiabatic cooling on the fitted parallel mean free path of solar energetic particles. *J. Geophys. Res.* 111, A08101. <https://doi.org/10.1029/2005JA011512>.
- Qin, G., Zhang, M., Dwyer, J.R., Rassoul, H.K., 2004. Interplanetary transport mechanisms of solar energetic particles. *Astrophys. J.* 609, 1076–1081. <https://doi.org/10.1086/421101>.
- Reames, D.V., 1999. Particle acceleration at the Sun and in the heliosphere. *Space Sci. Rev.* 90, 413–491. <https://doi.org/10.1023/A:1005105831781>.
- Reames, D.V., 2013. The two sources of solar energetic particles. *Space Sci. Rev.* 175, 53. <https://doi.org/10.1007/s11214-013-9958-9>.
- Reames, D.V., Richardson, I.G., Barbier, L.M., 1991. On the differences in element abundances of energetic ions from corotating events and from large solar events. *Astrophys. J.* 382, L43–L46. <https://doi.org/10.1086/186209>.
- Reid, G.C., 1964. A diffusive model for the initial phase of a solar proton event. *J. Geophys. Res.* 69, 2659–2667. <https://doi.org/10.1029/JZ069i013p02659>.
- Richardson, I.G., 2004. Energetic particles and corotating interaction regions in the solar wind. *Space Sci. Rev.* 111, 267. <https://doi.org/10.1023/B:SPAC.0000032689.52830.3e>.
- Roelof, E.C., 1969. Propagation of solar cosmic rays in the interplanetary magnetic field. In: Ögelman, H., Wayland, J.R. (Eds.), *Lectures in High-energy Astrophysics*, pp. 111.
- Ruffolo, D., 1995. Effect of adiabatic deceleration on the focused transport of solar cosmic rays. *Astrophys. J.* 442, 861–874. <https://doi.org/10.1086/175489>.
- Schwadron, N.A., Gorby, M., Török, T., Downs, C., Linker, J., Lionello, R., Mikić, Z., Riley, P., Giacalone, J., Chandran, B., Germaschewski, K., Isenberg, P.A., Lee, M.A., Lugaz, N., Smith, S., Spence, H.E., Desai, M., Kasper, J., Kozarev, K., Korreck, K., Stevens, M., Cooper, J., MacNeice, P., 2014. Synthesis of 3-D coronal-solar wind energetic particle acceleration modules. *Space Weather* 12, 323–328. <https://doi.org/10.1002/2014SW001086>.
- Shen, F., Feng, X., Song, W.B., 2009. An asynchronous and parallel time-marching method: application to three-dimensional MHD simulation of solar wind. *Sci. China E* 52, 2895–2902.
- Shen, F., Feng, X., Wu, S.T., Xiang, C., 2007. Three-dimensional MHD simulation of CMEs in three-dimensional background solar wind with the self-consistent structure on the source surface as input: numerical simulation of the January 1997 Sun-Earth connection event. *J. Geophys. Res.* 112, A06109. <https://doi.org/10.1029/2006JA012164>.
- Shen, F., Shen, C., Zhang, J., Hess, P., Wang, Y., Feng, X., Cheng, H., Yang, Y., 2014. Evolution of the 12 July 2012 CME from the Sun to the earth: data-constrained three-dimensional MHD simulations. *J. Geophys. Res.* 119, 7128–7141. <https://doi.org/10.1002/2014JA020365>.
- Shen, F., Yang, Z., Zhang, J., Wei, W., Feng, X., 2018. Three-dimensional MHD simulation of solar wind using a new boundary treatment: comparison with in situ data at earth. *Astrophys. J.* 866, 18. <https://doi.org/10.3847/1538-4357/aad806>.
- Skilling, J., 1971. Cosmic rays in the galaxy: convection or diffusion? *Astrophys. J.* 170, 265–273.
- Snodgrass, H.B., Ulrich, R.K., 1990. Rotation of Doppler features in the solar photosphere. *Astrophys. J.* 351, 309–316. <https://doi.org/10.1086/168467>.
- Sokolov, I.V., Roussev, I.I., Gombosi, T.I., Lee, M.A., Kóta, J., Forbes, T.G., Manchester, W.B., Sakai, J.I., 2004. A new field line advection model for solar particle acceleration. *Astrophys. J. Lett.* 616, L171–L174. <https://doi.org/10.1086/426812>.
- Tautz, R.C., Dosch, A., Lerche, I., 2012. Simulating cosmic-ray transport with adiabatic focusing. *Astron. Astrophys.* 545, A149. <https://doi.org/10.1051/0004-6361/201219636>.
- Totten, T.L., Freeman, J.W., Arya, S., 1995. An empirical determination of the polytropic index for the free-streaming solar wind using HELIOS 1 data. *J. Geophys. Res.* 100, 13–17. <https://doi.org/10.1029/94JA02420>.
- Wang, Y., Qin, G., 2016. Effects of adiabatic focusing on the diffusion of energetic charged particles. *Astrophys. J.* 820, 61. <https://doi.org/10.3847/0004-637X/820/1/61>.
- Wang, Y., Qin, G., Zhang, M., 2012. Effects of perpendicular diffusion on energetic particles accelerated by the interplanetary coronal mass ejection shock. *Astrophys. J.* 752, 37. <https://doi.org/10.1088/0004-637X/752/1/37>.
- Wiengarten, T., Kleimann, J., Fichtner, H., Kühl, P., Kopp, A., Heber, B., Kissmann, R., 2014. Cosmic ray transport in heliospheric magnetic structures. I. Modeling background solar wind using the CRONOS magnetohydrodynamic code. *Astrophys. J.* 788, 80. <https://doi.org/10.1088/0004-637X/788/1/80>.
- Wood, B.E., Howard, R.A., Thernisien, A., Socker, D.G., 2010. The three-dimensional morphology of a corotating interaction region in the inner heliosphere. *Astrophys. J. Lett.* 708, L89–L94. <https://doi.org/10.1088/2041-8205/708/2/L89>.
- Wu, Z., Chen, Y., Li, G., Zhao, L.L., Ebert, R.W., Desai, M.I., Mason, G.M., Lavraud, B., Zhao, L., Liu, Y.C.-M., Guo, F., Tang, C.L., Landi, E., Sauvaud, J., 2014. Observations of energetic particles between a pair of corotating interaction regions. *Astrophys. J.* 781, 17. <https://doi.org/10.1088/0004-637X/781/1/17>.
- Zhang, M., 1999. A Markov stochastic process theory of cosmic-ray modulation. *Astrophys. J.* 513, 409–420. <https://doi.org/10.1086/306857>.
- Zhang, M., Qin, G., Rassoul, H., 2009. Propagation of solar energetic particles in three-dimensional interplanetary magnetic fields. *Astrophys. J.* 692, 109–132. <https://doi.org/10.1088/0004-637X/692/1/109>.
- Zhao, L., Li, G., Ebert, R.W., Dayeh, M.A., Desai, M.I., Mason, G.M., Wu, Z., Chen, Y., 2016. Modeling transport of energetic particles in corotating interaction regions: a case study. *J. Geophys. Res.* 121, 77–92. <https://doi.org/10.1002/2015JA021762>.